

# Measured and modelled optical properties of particulate matter in the southern Benguela

S. Bernard<sup>a</sup>, T.A. Probyn<sup>b</sup> and R.G. Barlow<sup>b</sup>

Particulate absorption, particle size distributions and HPLC-derived pigments were used in combination with particle scattering models to examine the optical properties of natural algal assemblages in the southern Benguela. Inverse anomalous diffraction (IAD) models were used to derive the real and imaginary parts of the mean spherical equivalent particulate refractive index from absorption and particle size measurements. Such data were utilized with an homogeneous sphere Mie model to calculate particulate backscattering coefficients. The influence of natural particle size distributions on the ability of the IAD model to return unique refractive index values was assessed. Measured absorption and modelled backscattering coefficients, in addition to derived optical efficiency factors, were examined with regard to the influence of size, refractive index parameters and the variability of algal assemblages in the southern Benguela. The real part of the refractive index, as determined by the IAD model, was demonstrated to be a useful descriptor of algal assemblage structure. Significant non-linear relationships were established between the algal backscattering: absorption ratio and the real part of the particulate refractive index, indicating the potential to calculate the real part of the particulate refractive index from ocean colour data.

## Introduction

Ocean colour can be considered a spectral expression of the light near or leaving the surface of the sea, and can be described radiometrically as the reflectance<sup>1</sup>

$$R(\lambda) \equiv \frac{E_u(\lambda)}{E_d(\lambda)} \approx 0.33 \frac{b_b(\lambda)}{a(\lambda) + b_b(\lambda)}, \quad (1)$$

where  $R$  is the irradiance reflectance,  $E_u$  is the upwelling irradiance ( $W\ m^{-2}$ ),  $E_d$  is the downwelling irradiance ( $W\ m^{-2}$ ),  $b_b$  is the total backscattering coefficient ( $m^{-1}$ ),  $a$  is the absorption coefficient ( $m^{-1}$ ), and  $\lambda$  indicates wavelength dependency (nm). Seawater and its constituents thus affect ocean colour in a quantifiable manner through the absorption and backscattering coefficients, as given by the above expression. These coefficients form part of a suite of inherent optical properties (IOPs),<sup>2</sup> which are independent of the submarine light field, and can therefore be used to characterize a hydrosol optically. In the highly productive coastal waters of the Benguela system, phytoplankton comprise a collective hydrosol of considerable ecological importance. Ocean colour measurements can therefore provide a powerful tool for ecological studies of the southern Benguela, if the processes governing the regional optical properties of phytoplankton can be understood.

While the absorption coefficient of suspended particulate

matter can be relatively easily measured with the filter pad technique,<sup>3,4</sup> backscattering has historically been difficult to quantify directly.<sup>5</sup> An alternative approach to direct measurement is the use of physically based models, through which the attenuation and scattering of electromagnetic radiation incident on a particle population can be calculated. Inverse anomalous diffraction<sup>6</sup> models can be used to derive mean refractive index data for particle populations<sup>7,8</sup> and, given these data, particulate backscattering coefficients can be calculated using Mie theory. Such models have been used extensively with cultured phytoplankton samples<sup>5,9,10</sup> and they were used here to calculate refractive index and backscattering data for natural particle assemblages.

The assumption of homogeneous spherical particles made in these models has the effect of reducing the optical determinants of a cell population to the particle size distribution and the bulk refractive index.<sup>8</sup> The refractive index, a mean value calculated for an equivalent spherical particle population, is a complex number, typically denoted as

$$m(\lambda) = n(\lambda) \pm i\kappa(\lambda), \quad (2)$$

where  $n$  is the real part of the index,  $\kappa$  is the imaginary part of the index or the absorption index,<sup>11</sup>  $\lambda$  is the wavelength and  $i = \sqrt{-1}$ . The bulk refractive index is in itself a useful optical variable for characterizing a particle population, and its determination, from particulate absorption and particle size measurements, forms the first step of the modelling process presented here. Good correlations have been shown between the real part of the refractive index  $n$  and intracellular carbon concentration, and between the imaginary part of the refractive index  $\kappa$  and intracellular chlorophyll  $a$  concentration.<sup>12</sup> The influence of the particle size distribution and the refractive index parameters  $n(\lambda)$  and  $\kappa(\lambda)$  upon the backscattering coefficient are theoretically predictable, but they are intricate, simultaneously dependent and vary spectrally.<sup>7</sup> Analysis of the relationship between backscattering and particle characteristics thus requires full computation of angular scattering across the visible spectrum using Mie theory.

There are drawbacks to this approach, arising primarily from the assumption of homogeneous spherical particles such models make. Phytoplankton are considerably more complex in shape and structure, and divergences between measured and modelled angular scattering (employing homogeneous spherical particles) have been reported for cultured phytoplankton.<sup>13,14</sup> However, such an approach represents a good first approximation<sup>9</sup> and allows an understanding of the effects of particle characteristics on scattering behaviour.

Using this approach, the processes controlling the bulk particulate absorption and backscattering coefficients can be examined. In addition, the optical properties at the cellular level can be considered, or, more accurately in the case of polydispersed populations, a 'mean' cell representing the population. The optical properties of such a mean cell can be represented by dimensionless optical efficiency factors, which are related to the bulk coefficients through the following relationship<sup>9</sup>:

<sup>a</sup>Department of Oceanography, University of Cape Town, Private Bag, Rondebosch, 7701 South Africa.

<sup>b</sup>Marine and Coastal Management, Private Bag X2, Rogge Bay, 8012 South Africa.

\*Author for correspondence. E-mail: bernard@physci.uct.ac.za

$$a = \frac{\pi}{4} \overline{Q}_a \int_0^{\infty} F(d) d^2 d(d), \quad b_b = \frac{\pi}{4} \overline{Q}_{b_b} \int_0^{\infty} F(d) d^2 d(d), \quad (3)$$

where  $a$  is the absorption coefficient,  $b_b$  is the backscattering coefficient,  $\overline{Q}_a$  is the mean absorption efficiency factor,  $\overline{Q}_{b_b}$  is the mean backscattering efficiency factor,  $d$  is the particle diameter, and  $F(d)d(d)$  is the number of particles per unit volume in the size range  $d \pm \frac{1}{2}d(d)$ . A particle modelling approach therefore provides a means of considering three aspects of particle optics: the underlying physical phenomena, that is, refractive index and size, the optical efficiency factors of a 'mean' cell, and the bulk absorption and backscattering coefficients that are responsible for modifying the marine light field. It is these bulk coefficients that are of particular importance to the analysis of ocean colour data [Equation (1)]. The parameterization of these coefficients allows the regional application of analytical models to ocean colour data, either with satellite-derived synoptic colour observations,<sup>15</sup> or with *in situ* data for the purposes of detecting harmful algal blooms.<sup>16</sup> Such models, or bio-optical algorithms, should offer a greater depth of information regarding algal dynamics than empirically derived pigment algorithms, provided that the IOPs central to these models can be regionally constrained.

A preliminary study of the characteristics of the particulate absorption and backscattering coefficients was made using data from the southern Benguela in conjunction with anomalous diffraction and Mie models. Inverse anomalous diffraction (IAD) models have previously been applied to cultured phytoplankton samples.<sup>7,8</sup> In our study, the performance of these models was assessed with regard to natural assemblages. The relationship between IOPs, pigment concentration, derived refractive index parameters, and particle size descriptors is examined, with the purpose of establishing criteria that may be used to parameterize these variables.

**Materials and methods**

Data were gathered on Leg 1 of the June 1999 BENEFIT research training cruise aboard the *FRS Africana*, between Cape Town and Walvis Bay.<sup>37</sup> Samples from ten stations, taken from depths between the surface and 40 m, were analysed for particulate absorption spectra, particle size counts, and cellular pigment data. Station positions are shown in Fig. 1; it can be seen that most stations were located in inshore coastal waters, with the exception of two stations (b0502 and b0503) placed approximately 200 km off the Orange River mouth.

**Absorption**

Particulate absorption data were measured using the filter pad technique<sup>4,17</sup> on a Shimadzu UV-2501 spectrophotometer equipped with an ISR-2200 internal integrating sphere. Briefly, seawater was gently filtered onto Whatman GF/F filter pads, which were placed at the entrance port of the sphere, and scanned from 350 nm to 750 nm using an air reference and baseline. Blank filter pads were prepared by filtering several hundred millilitres of pre-filtered seawater through fresh GF/F filters, which were then read in the same manner as the samples. Raw optical density values at 438 nm, corrected for blank absorption, ranged from 0.7 (surface sample with 500 ml filtered) to 0.07 (40-m sample with 2000 ml filtered). Detrital corrections were made where appropriate using methanol extraction on the filter, followed by re-reading in the spectrophotometer.<sup>18</sup> Absorption coefficients were calculated using the path-length amplification factor of Roesler.<sup>17</sup> Spectra were digitally filtered using an FIR filter (Finite Impulse Response, 30 point Hamming window,

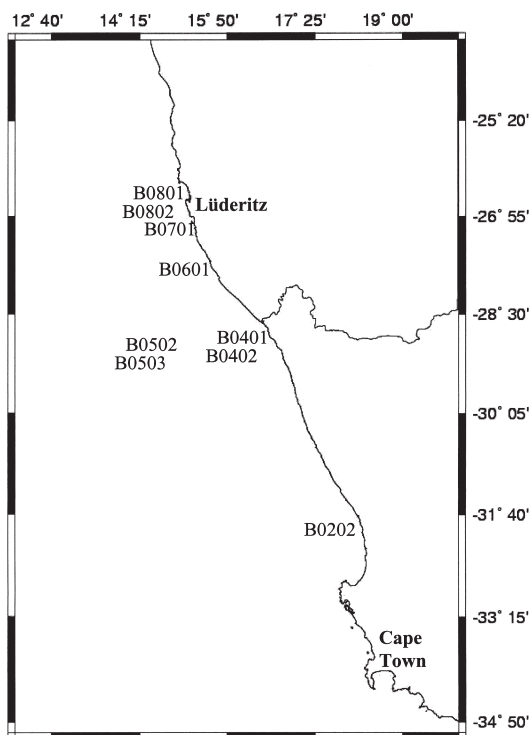


Fig. 1. Location of sampling sites in the southern Benguela.

Matlab, The Mathworks), resampled from 0.2 nm to 4 nm spectral resolution, and corrected with the assumption that particulate absorption at 750 nm is zero.<sup>17</sup>

**Particle size distribution (PSD)**

Particle size measurements were made using a 128-channel Coulter Multisizer II with a 140- $\mu$ m aperture in manometer mode, using freshly prepared, 0.2- $\mu$ m filtered seawater as both blank and electrolyte. Samples were diluted to keep coincidence levels below 10%, and 40 ml of sample was typically counted. It should be noted that the Coulter counter technique calculates particle diameter assuming an equivalent volume sphere. Coincidence-corrected cell counts in cells per litre were median filtered to remove electronic spiking, and interpolated to 0.2- $\mu$ m diameter size bins. The confident particle diameter range using a 140- $\mu$ m aperture was restricted from 3.4  $\mu$ m to 70  $\mu$ m. However, corresponding absorption measurements were made using a GF/F filter, which had a nominal pore size of  $\sim$ 0.6  $\mu$ m. To overcome this discrepancy, PSD spectra were curve-fitted to a combination of a Jungian distribution<sup>19</sup> and up to four log-normal distributions<sup>20</sup> using Peakfit v4.04 (Jandel Scientific). In all cases the fits were good ( $r^2 > 0.99$ ), and the fitted curves were used to extrapolate the PSD spectra to a diameter of 0.6  $\mu$ m, corresponding to nominal GF/F pore size. Further description of the PSD spectra included calculating the effective radius  $r_{eff}$  and effective variance  $v_{eff}$ <sup>21</sup> for each size distribution. These parameters are defined as follows:

$$r_{eff} = \frac{\int_{r_1}^{r_2} r \pi r^2 F(r) dr}{\int_{r_1}^{r_2} \pi r^2 F(r) dr} = \frac{1}{G} \int_{r_1}^{r_2} r \pi r^2 F(r) dr \quad (4)$$

$$v_{eff} = \frac{1}{G r_{eff}^2} \int_{r_1}^{r_2} (r - r_{eff})^2 \pi r^2 F(r) dr \quad (5)$$

where  $F(r)$  is the number of particles of radius  $r$  in the radius interval  $dr$ ,  $r_1$  and  $r_2$  are the minimum and maximum radius

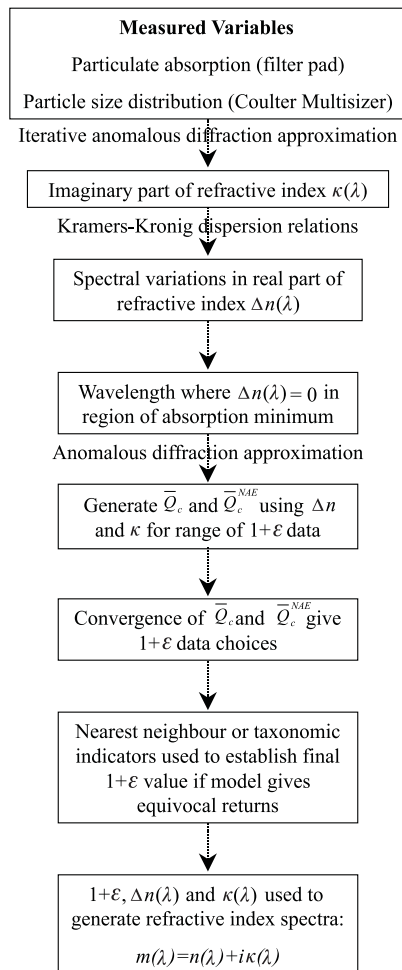


**Fig. 2.** Schematic representation of the Inverse Anomalous Diffraction (IAD) modelling scheme used to derive information on refractive index from measured absorption and particle size distribution data.

evaluated, and  $G$  is the geometrical cross-sectional area of particles per unit volume. As particles scatter light proportional to  $\pi r^2$ , the effective radius and variance reflect the 'mean' size and width of the size distribution of scattering particles, respectively. These parameters have been used previously to describe phytoplankton particle optics,<sup>14</sup> and are described as 'the primary characteristics of essentially any physically plausible size distribution of spherical particles'.<sup>22</sup>

### Pigments

Pigments were analysed by filtering water samples onto Whatman GF/F filters under gentle vacuum, after which they were frozen in liquid nitrogen and analysed using high-performance liquid chromatography.<sup>23</sup>

### Refractive index modelling and determination

The complex refractive index was determined using a combination of published methods<sup>7,8</sup> with some variations to allow for simpler computations and lack of measured attenuation data. A schematic outline of the computational methods employed is presented in Fig. 2.

The imaginary part of the refractive index  $\kappa(\lambda)$  was determined using the iterative technique of Bricaud and Morel,<sup>7</sup> using measured total particulate absorption coefficients and PSD data processed as above. The detrital correction was not used for the absorption data as an equivalent correction was not possible for the corresponding PSD data. Equivalent particle populations

are required for the validity for any calculations involving both absorption and PSD data, and thus detrital corrections could not be applied. The refractive index, optical efficiency and scattering data presented here are therefore representative of the total suspended particulate load, and not phytoplankton alone, as defined by the methods of Kishino *et al.*<sup>18</sup>  $\kappa(\lambda)$  data were calculated in 4-nm wavelength spacings from 350 nm to 750 nm.

The next step in refractive index determination was the calculation of the spectral variations in the real part of the index, typically denoted as  $\Delta n(\lambda)$  from the imaginary part of the index.<sup>7</sup> In this study, the Kramers-Kronig (KK) relations<sup>24</sup> were used as a replacement for the Ketteler-Helmholtz theory that employs the Lorentzian oscillators of Bricaud and Morel.<sup>7</sup> The KK relations describe the mutual dependence of the real and imaginary parts of the refractive index through dispersion, as does Ketteler-Helmholtz theory,<sup>24</sup> but they are more simply applied than the tedious and sometimes inaccurate use of summed oscillators.<sup>8</sup> Computational difficulties in the KK relations, specifically the evaluation of the Cauchy principal integral, were overcome using a Hilbert transform in Matlab on the imaginary part of the refractive index to calculate  $\Delta n(\lambda)$ . The scheme was verified by comparison with  $\Delta n(\lambda)$  determinations using Lorentzian oscillators and the KK relations on the same  $\kappa(\lambda)$  data. Figure 3 shows such a comparison using a simplified situation of two Lorentzian oscillators, as opposed to the 9–15 oscillators typically used for phytoplankton samples.<sup>7,8</sup> These illustrative  $\kappa$  oscillators are centred at 500 nm and 600 nm, and are set to have peak amplitudes of 0.005, comparable in magnitude to phytoplankton samples.<sup>5</sup> The sum of these oscillators was treated as the effective  $\kappa(\lambda)$  from which the KK-derived  $\Delta n(\lambda)$  was calculated. The Lorentzian derived  $\Delta n(\lambda)$  was calculated as per Bricaud and Morel.<sup>7</sup> Figure 3 illustrates the difficulty of reconstructing very low values of  $\kappa(\lambda)$  using Lorentzian oscillators,<sup>8</sup> resulting from the long tails of the Lorentzian function. The KK relations provide an advantage in this case, as no  $\kappa(\lambda)$  reconstruction is necessary. The  $\Delta n(\lambda)$  values from the two methods are similar in shape, with the results of anomalous dispersion evident at the wavelengths of the  $\kappa(\lambda)$  peaks. The Lorentzian method produces larger values at the edges of the spectral domain where  $\kappa(\lambda)$  values are lowest. The reasons for this are unclear and beyond the scope of this study. Suffice it to say that the KK relations are expressions governing the dependence of real and imaginary parts of the refractive index based on causality, whereas the Lorentzian approach can be used to simulate the same dependence. On a fundamental level, the Lorentzian model should conform to the KK relations rather than *vice versa*.<sup>24</sup>

The final part of the refractive index determination was the choice of the central value of the real part of the index — essentially fixing the absolute magnitude of  $n(\lambda)$  around which  $\Delta n(\lambda)$  varies. This variable is denoted as  $1+\epsilon$ .<sup>7</sup> For phytoplankton it typically ranges from 1.02 to 1.15, relative to water.<sup>7,11</sup> The computation of  $1+\epsilon$  is relatively straightforward if attenuation data are available.<sup>8</sup> Unfortunately, no such data were available, so the computational scheme of Stramski *et al.*<sup>8</sup> was modified. In the  $\Delta n(\lambda)$  spectra there are several instances of  $\lambda$  where  $\Delta n = 0$ .<sup>8</sup> In all but one case examined, three of these wavelengths occurred, at approximately 440 nm, 650 nm and 670 nm. At these wavelengths the mean attenuation efficiency factors  $\bar{Q}_c$  and  $\bar{Q}_c^{NAE}$ , where  $\bar{Q}_c^{NAE}$  represents a non-absorbing equivalent population, were generated using  $\kappa(\lambda)$ ,  $\Delta n(\lambda)$  and a range of  $1+\epsilon$  values between 1.02 and 1.12, based on anomalous diffraction relations.<sup>7</sup> This differs from the scheme of Stramski *et al.*<sup>8</sup> in that  $\bar{Q}_c$  is not an 'experimental' parameter, but a modelled one. The value of  $1+\epsilon$  was then determined such that  $\bar{Q}_c = \bar{Q}_c^{NAE}$ . These

**Table 1.** Intracellular pigment concentrations and particle size characteristics of all samples. The shaded box indicates offshore stations.

Station/depth	Biomass Chl a [mg m <sup>-3</sup> ]	Diatom presence Fuc/Chl a	Pyrmnes presence Hex/Chl a	Chlorophyte presence Chl b/Chl a	Dinoflagellate presence Per/Chl a	Effective radius or mean size of PSD <i>r</i> <sub>eff</sub> [μm]	Effective variance or width of PSD <i>v</i> <sub>eff</sub>
b0202/0 m	3.02	0.22	0.29	0.11	0.06	1.72	3.34
b0202/17 m	2.92	0.25	0.33	0.12	0.05	1.84	2.98
b0202/30 m	2.16	0.25	0.31	0.11	0.04	1.67	4.00
b0202/40 m	0.20	0.42	0.06	0.00	0.10	7.12	1.24
b0302/0 m	3.69	0.35	0.30	0.07	0.07	2.46	2.13
b0302/10 m	3.65	0.34	0.28	0.07	0.08	2.18	2.20
b0302/20 m	1.01	0.39	0.11	0.06	0.21	3.40	1.98
b0302/25 m	1.09	0.44	0.01	0.03	0.20	3.65	1.42
b0401/0 m	13.63	0.44	0.02	0.02	0.05	4.98	1.31
b0402/0 m	6.24	0.36	0.16	0.06	0.08	3.24	1.33
b0402/8 m	6.18	0.35	0.17	0.05	0.09	3.41	1.25
b0402/16 m	3.13	0.42	0.10	0.05	0.04	2.37	2.42
b0402/20 m	1.83	0.48	0.06	0.04	0.03	2.35	2.51
b0502/0 m	0.59	0.09	0.03	0.18	0.05	3.21	1.40
b0502/13 m	0.58	0.08	0.45	0.17	0.05	3.06	1.22
b0502/28 m	0.59	0.09	0.43	0.20	0.04	3.53	1.72
b0503/0 m	0.57	0.08	0.58	0.16	0.02	2.89	2.41
b0503/13 m	0.60	0.08	0.62	0.17	0.02	2.44	2.10
b0503/28 m	0.60	0.09	0.60	0.17	0.02	2.23	2.37
b0601/0 m	0.57	0.32	0.13	0.04	0.14	5.32	1.05
b0701/0 m	0.53	0.28	0.02	0.11	0.02	2.04	2.81
b0801/0 m	5.82	0.41	0.00	0.00	0.00	8.01	1.33
b0802/0 m	5.28	0.37	0.00	0.02	0.00	4.69	1.53
Minimum	0.20	0.08	0.00	0.00	0.00	1.67	1.05
Maximum	13.63	0.48	0.62	0.20	0.21	8.01	4.00
Mean (s.d.) inshore	3.58 (3.27)	0.36 (0.08)	0.14 (0.12)	0.06 (0.04)	0.07 (0.06)	3.55 (1.89)	2.05 (0.86)
Mean (s.d.) offshore	0.59 (0.01)	0.08 (0.00)	0.45 (0.22)	0.18 (0.01)	0.04 (0.01)	2.96 (0.60)	1.82 (0.53)

potential  $1+\epsilon$  values, as indicated by the refractive index model, will be termed ‘convergences’ in further discussion. Rather than using the mean of the three wavelengths where  $\Delta n = 0$ ,<sup>8</sup> a single wavelength was used where  $\kappa(\lambda)$  is a minimum. The rationale for this choice is that  $\bar{Q}_c$  and  $\bar{Q}_c^{NAE}$  should be most similar in that part of the spectrum where absorption effects are lowest. In this study, the wavelength at this point where  $\Delta n = 0$  and  $\kappa(\lambda)$  was minimal ranged between 642.4 nm and 656.2 nm (Table 2). The resulting  $1+\epsilon$  values returned by the IAD model fell into three categories, as dictated by model convergence:

1. A single unequivocal  $1+\epsilon$  value was returned from a single convergence.
2. The model converged at several  $1+\epsilon$  values. This resulted from the fact that the  $\bar{Q}_c$  and  $\bar{Q}_c^{NAE}$  functions are not monotonic with respect to  $1+\epsilon$  particularly at larger cell sizes.<sup>8</sup> In these

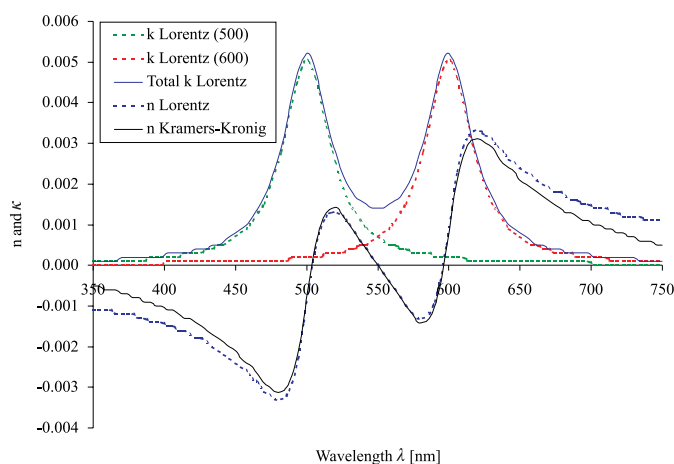


**Fig. 3.** Comparison of the real  $n(\lambda)$  and imaginary  $\kappa(\lambda)$  parts of the refractive index for the Kramers-Kronig relations (solid lines) and Ketteler-Helmholtz theory (dashed lines). Two Lorentzian oscillators were used to construct illustrative spectra for the imaginary part of the refractive index.

3. The model does not converge. Bricaud and Morel<sup>7</sup> noted that a similar method fails for large cells with a wide polydispersion. In cases where a ‘nearest neighbour’ produced an unequivocal value, this value was taken for  $1+\epsilon$  and indicated as a ‘nearest neighbour value’. In cases where there was no ‘nearest neighbour’, the mean value of all  $1+\epsilon$  values (1.036) was used as a default.

Further discussion of the performance of the IAD model is provided in the context of the full modelling results.

**Mie modelling**

The Agaus model (A. Miller, Department of Physics, New Mexico State University) was used to describe particulate attenuation  $c(\lambda)$ , scattering  $b(\lambda)$ , absorption  $a(\lambda)$ , and phase function  $\tilde{\beta}(\lambda)$ , given inputs of refractive index parameters  $n(\lambda)$  and  $\kappa(\lambda)$  and the particle size distribution. Particulate backscattering  $b_b(\lambda)$  data were then calculated using the following expression:

$$b_b(\lambda) = 2\pi b(\lambda) \int_{\pi/2}^{\pi} \tilde{\beta}(\lambda, \theta) \sin\theta d\theta \tag{6}$$

where  $\theta$  is the scattering angle relative to incident direction. The quality of the angular scattering calculation was checked with the following expression:<sup>26</sup>

$$2\pi \int_0^{\pi} \tilde{\beta}(\lambda, \theta) \sin\theta d\theta = 1. \tag{7}$$

**Table 2.** Refractive index characteristics and performance of the inverse anomalous diffraction model (IAD) for all samples. The convergences column indicates all possible values of 1+ε returned by the IAD model.

Station / depth	κ(β74)		Δn = 0 wavelengths (nm)		Convergences		1+ε chosen		Reason for 1+ε choice
	Soret peak region	a <sub>p</sub> (minimum) region	Red chl a peak region	a <sub>p</sub> (minimum) region	Soret peak region	a <sub>p</sub> (minimum) region	Red chl a peak region	1+ε chosen	
b0202/0 m	0.0019	446.3	669.8	652.1	-	-	-	1.036	Mean of all values
b0202/17 m	0.0034	442.0	669.8	653.8	-	-	-	1.036	Mean of all values
b0202/30 m	0.0028	442.4	669.7	653.7	-	-	-	1.036	Mean of all values
b0202/40 m	0.0004	423.8	-	-	1.020, 1.029, 1.065	-	-	1.029	Nearest-neighbour convergence
b0302/0m	0.0040	443.5	670.8	652.6	-	1.035	1.021, 1.035	1.035	Single convergence
b0302/10 m	0.0044	443.2	670.6	651.6	-	1.034	1.022, 1.034	1.034	Single convergence
b0302/20 m	0.0052	434.0	670.8	654.3	-	1.033, 1.057, 1.068	1.034, 1.06, 1.069	1.033	Nearest-neighbour convergence
b0302/25 m	0.0042	429.0	671.0	652.3	1.021	1.034, 1.056, 1.069	1.035, 1.059, 1.071	1.034	Nearest-neighbour convergence
b0401/0 m	0.0024	440.2	670.3	644.7	1.023	1.033	1.035	1.033	Single convergence
b0402/0 m	0.0016	443.0	670.0	649.1	1.029	1.043	1.045	1.043	Single convergence
b0402/8 m	0.0020	443.5	669.8	648.7	1.031	1.045	1.046	1.045	Single convergence
b0402/16 m	0.0024	440.5	669.6	648.8	-	1.023	-	1.023	Single convergence
b0402/20 m	0.0023	435.0	669.4	650.9	-	1.024	1.021, 1.024	1.024	Single convergence
b0502/0 m	0.0015	434.3	666.2	661.7	1.035	1.055	1.055	1.055	Single convergence
b0502/13 m	0.0025	441.3	668.8	654.8	1.035	1.055	1.056	1.055	Single convergence
b0502/28 m	0.0017	441.7	668.8	654.5	1.032	1.049	1.050	1.049	Single convergence
b0503/0 m	0.0039	439.8	669.7	656.2	-	1.026, 1.030	1.024, 1.039	1.030	Nearest-neighbour convergence
b0503/13 m	0.0024	442.7	669.3	654.3	-	1.028	-	1.028	Single convergence
b0503/28 m	0.0027	443.9	668.2	655.8	-	-	-	1.028	Nearest-neighbour value
b0601/0 m	0.0019	438.1	670.9	647.4	1.027, 1.049, 1.054	1.040, 1.069, 1.082	1.042, 1.072, 1.085	1.040	Taxonomy convergence
b0701/0 m	0.0012	425.4	668.8	652.2	-	-	-	1.036	Mean of all values
b0801/0 m	0.0032	432.7	671.1	643.9	-	1.020, 1.033, 1.038	1.021, 1.036, 1.038	1.020	Taxonomy convergence
b0802/0 m	0.0054	434.0	671.1	642.4	-	1.022	1.023	1.022	Single convergence

No sample evaluated had a value larger than 1.03, indicating that both the angular resolution and size integrations in the Mie model were not aliased by spiking.<sup>27</sup> Optical efficiency factors  $\bar{Q}_a$  and  $\bar{Q}_b$  were calculated using Equation (3) and measured absorption data, measured PSD data, and modelled particulate backscattering data. In addition to these, the 'package effect'  $Q_a^*$ , which can be quantified as the ratio of the absorption of pigmented cells to the absorption of the same cellular material dispersed into solution, was calculated using<sup>28</sup>

$$Q_a^* = \frac{3Q_a(\rho')}{2\rho'} \quad (8)$$

where  $\rho'$  is the optical thickness and is given by  $\rho' = a_{cm}d$ , where  $a_{cm}$  is the absorption coefficient of the cellular matter. The 'package effect' parameter  $Q_a^*$  allows an analysis of the effects of cell packaging (cell size and intracellular pigment concentration) upon particulate absorption.<sup>28</sup>

## Results and discussion

### Cell size, pigments and community structure

Samples of the measured particle size distributions are shown in Fig. 4, for depth profiles from stations b0402 and b0502, inshore and offshore, respectively, of the Orange River. Table 1 details  $r_{eff}$  and  $v_{eff}$  for all samples analysed. The samples displayed appreciable structure within the particle community, with significant changes through the water column. A Jungian distribution,<sup>29</sup> often used as an approximation for the marine particle size distribution,<sup>26</sup> of arbitrary magnitude was plotted for reference. It should be appreciated that Fig. 4 shows the volume particle size distribution. The  $r_{eff}$  values range from 1.67  $\mu\text{m}$  (mixed assemblage) to 8.01  $\mu\text{m}$  (diatom assemblage) and  $v_{eff}$  ranges from 1.05 to 4.00, all of which are higher than the  $v_{eff}$  values of Volten *et al.*<sup>14</sup> for cultured phytoplankton. This is to be expected and results from the predominance of small particles, and mixed phytoplankton communities, found in natural assemblages. Likewise, the predominance of small particles affects the  $r_{eff}$  values, with only three of the 23 samples having  $r_{eff} > 5 \mu\text{m}$  despite appreciable particle populations at larger sizes (e.g. sample b0401 had a particle concentration of  $\sim 200\ 000$  cells per litre between 9 and 11  $\mu\text{m}$ , with  $r_{eff} = 4.98$ ).

Chemotaxonomic analysis of the samples (Table 1) can be effected using pigment concentrations: the ratios of fucoxanthin (fuc), 19'-hexanoyloxyfuc-

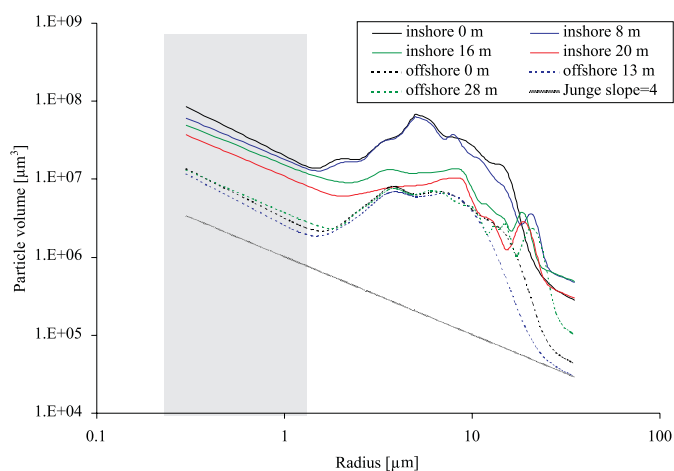


**Fig. 4.** Illustrative particle size distribution (PSD) spectra for inshore station b0402 and offshore station b0502. PSD spectra are displayed as particle volume, and the shaded box indicates the size range where extrapolation based on curve fitting was used to extend the PSD size range to 0.6  $\mu\text{m}$ . A Jungian size distribution of arbitrary magnitude is shown for comparison.

xanthin (hex), chlorophyll *b* (chl *b*) and peridinin (per) to chlorophyll *a* (chl *a*). It is possible to use these pigment ratios as bio-markers,<sup>23</sup> indicating the relative abundance of diatoms (fuc), prymnesiophytes (hex), chlorophytes and prasinophytes (chl *b*) and dinoflagellates (per). Differences in community structure were most apparent between the six samples taken offshore and the remaining inshore stations. The inshore stations typically showed diatom dominance through relatively high fuc:chl *a* ratios, with a variable prymnesiophyte presence, with maximal biomass near the surface. Inshore stations displayed little evidence of chlorophyte presence, and higher, more variable chl *a* concentrations. By contrast, the offshore samples showed lower, less variable chl *a* concentrations and diatom presence, and a higher prymnesiophyte and chlorophyte presence. In addition, the two offshore stations presented here showed little gross biomass structure through the upper water column. Offshore waters therefore appeared to be dominated by prymnesiophyte/chlorophyte populations, while the more productive shelf waters typically displayed diatom dominance with greater community variability, as indicated by both pigment and cell size parameters. The findings of Barlow *et al.*<sup>23</sup> support such a scenario.

**Particulate refractive indices**

Results of the refractive index modelling are shown in Table 2, detailing the response of the model to all samples and the rationale behind the  $1+\epsilon$  choice where model output was equivocal. Of the 23 samples analysed, the IAD model returned unequivocal  $1+\epsilon$  values on 12 occasions, equivocal  $1+\epsilon$  values on six occasions, and failed to converge five times. Figure 5a details the three types of model return plotted in effective radius/effective variance space. The model appears to fail to converge when the PSD was broadly polydispersed and featureless (relative to a Jungian distribution), i.e. when  $v_{\text{eff}}$  was relatively high ( $>2.3$ ) and  $r_{\text{eff}}$  was relatively low ( $<\sim 2.2\mu\text{m}$ ). Bricaud and Morel<sup>7</sup> noted that similar methods for determining  $1+\epsilon$  fail for large polydispersed cells. It appeared that highly polydispersed particle populations, even with a small mean particle size, also did not show a sufficient dependency between attenuation efficiency and  $1+\epsilon$  for the refractive index to be determined in this manner.

The effect of the PSD on the ability of the model to return a more desirable single  $1+\epsilon$  value over multiple  $1+\epsilon$  values is less

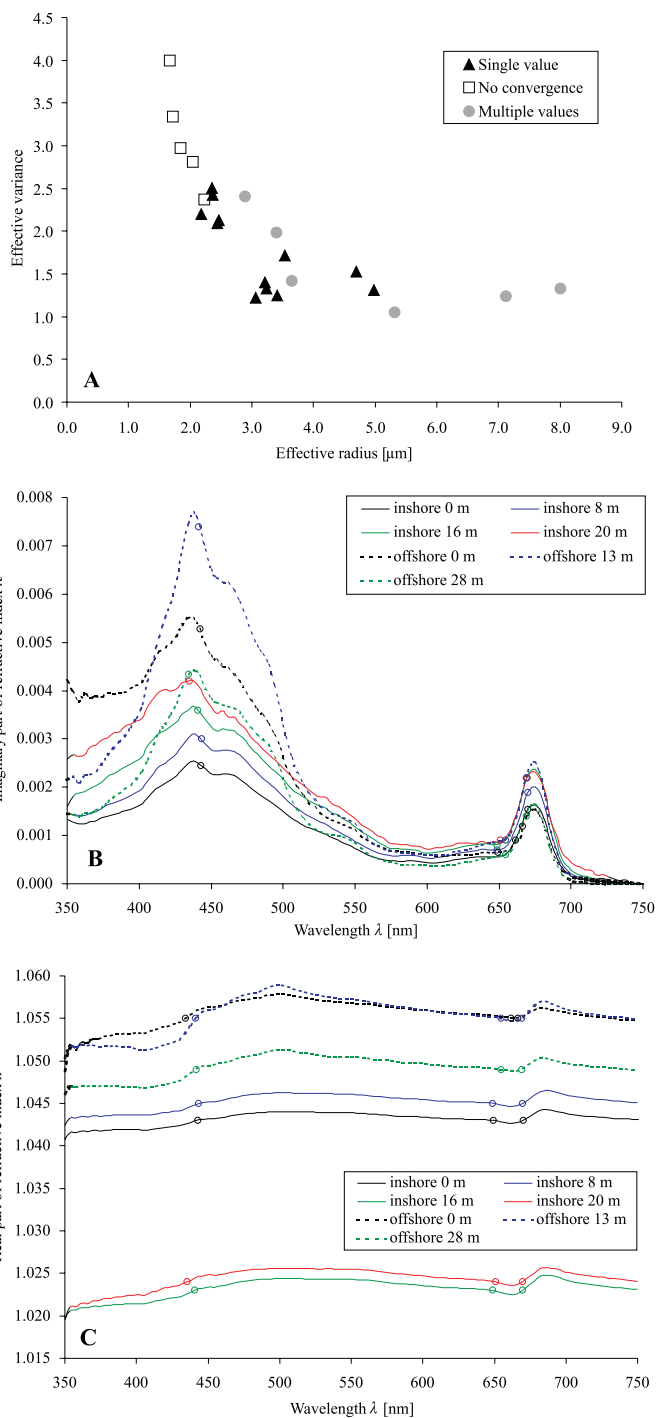


**Fig. 5.** Performance and results of the inverse anomalous diffraction model: **a**, returned  $1+\epsilon$  values from the IAD model plotted in effective radius/effective variance space for all samples; **b**, imaginary part of the refractive index  $\kappa(\lambda)$  for the two example stations; and **c**, real part of the refractive index  $n(\lambda)$  for the two illustrative stations. The circles indicate wavelengths where  $\Delta n = 0$ .

easy to characterize. It appears that populations with a large mean cell size do not return unequivocal  $1+\epsilon$  values, even with relatively narrow size distributions (samples b0202/40 m, b0601/0 m and b0801/0 m). This is not unexpected: Stramski *et al.*<sup>8</sup> noted that at large particle sizes the attenuation efficiency factor  $Q_c$  becomes independent of size/refractive index parameters. Multiple model returns are not restricted only to populations with large mean cell sizes. There is another dependency of the model upon  $\kappa(\lambda)$  and therefore  $\Delta n(\lambda)$ . However, evaluation of model performance is restricted to the more simply analysed

influences of the particle size distribution.

Sample  $\kappa(\lambda)$  and  $n(\lambda)$  spectra are shown in Figs 5b and 5c, respectively, for the two stations examined in Fig. 3 (inshore and offshore stations at the Orange River latitude). All of these samples produced unequivocal  $1+\varepsilon$  returns from the IAD model. There was appreciable variation in  $\kappa(\lambda)$ , spectrally and in magnitude, between samples. It appears that smaller cells (offshore), associated with lower biomass, typically displayed high  $\kappa(\lambda)$  values. The  $n(\lambda)$  values (whose spectral variations are linked to  $\kappa(\lambda)$  through the KK relations) displayed marked changes in magnitude with depth and trophic state (Fig. 5c). The inshore station revealed that two algal populations could be identified on the basis of  $n(\lambda)$  values: a surface population (0–8 m) with  $n \approx 1.045$  and a deeper population (16–20 m) with  $n \approx 1.025$ . The pigment data support this identification (Table 1), showing an increase with depth in the relative diatom composition and a decrease in the relative prymnesiophyte composition.

The returned  $n$  values are consistent with published data indicating that diatoms are 'soft' cells, i.e. have relatively low  $n$  values of  $\sim 1.02$ .<sup>11,25,14</sup> The offshore station (for the upper 28 m) revealed less variability in the magnitude of  $n$ , although spectral variations in both  $\kappa(\lambda)$  and  $n(\lambda)$  can be observed. The pigment data again indicated a change in population composition with depth — the surface sample appeared to be a mixed population, whereas the two deeper samples were prymnesiophyte dominated.

#### Optical efficiency factors

The optical efficiency factors  $\bar{Q}_a$  [Equation (3)] and  $Q_a^*$  [Equation (8)] are displayed in Figs 6a and 6b, respectively, for the stations previously discussed. Data for all samples are shown in Table 3.

The  $\bar{Q}_a$  spectra (Fig. 6a) support the hypothesis that four distinct populations (inshore surface and deep, offshore surface and deep) existed during sampling. The more pronounced absorption feature at 550 nm in the offshore samples is likely to be caused by the presence of phycoerythrin-containing species.<sup>30</sup> This is confirmed by independent chemotaxonomic analysis (Fig. 2, ref. 23). In addition, spectral differences between the surface and deep samples for both stations can be observed in the  $\bar{Q}_a$  spectra, consistent with pigment and refractive index analyses. The range of  $\bar{Q}_a$  (674) values reported in Table 3 (0.05–0.39) is in agreement with previous studies for cultured phytoplankton.<sup>5,25</sup>

The package effect ( $Q_a^*$ )<sup>31,28</sup> arises from the containment of pigment within the cell, and is typically manifest as a flattening of the absorption spectra in comparison to the spectra of the same cellular material ideally dispersed into solution. Values of  $Q_a^*$  for the sample stations are displayed in Fig. 6b, and again demonstrate the variability in assemblage properties. The package effect is influenced by cell size, here given by  $r_{\text{eff}}$ , and the absorption of cellular material, which can be taken here as proportional to  $\kappa$ .<sup>25</sup> These effects are particularly noticeable in the upper two depths at both stations. Despite these samples having approximately similar  $r_{\text{eff}}$  values, the offshore stations display enhanced package effects in the blue region, consistent with their enhanced  $\kappa$  values in this part of the spectrum. Further investigation of the relationship between mean cell size, as given by  $r_{\text{eff}}$ , and the package effect is shown in Fig. 6c. Results for three wavelengths are used for 22 samples with b0202/40 m excluded as an outlier. The area of the blue absorption maxima is represented by 442 nm, the absorption minima by 622 nm (corresponding to the 620-nm band of the Medium Resolution Imaging Spectrometer, MERIS<sup>32</sup>), and the red chlorophyll *a* absorption band by 674 nm. Figure 6c shows that over 83% of

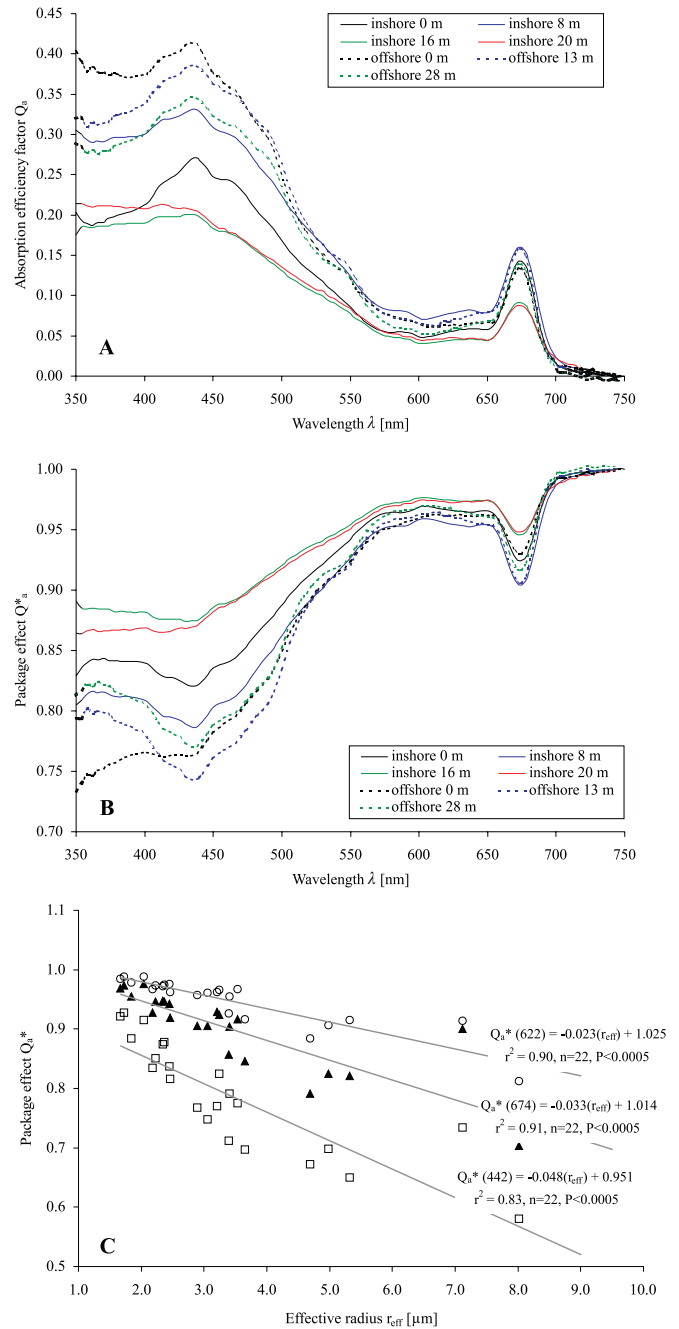


**Fig. 6.** Mean particulate optical efficiency factors: **a**, absorption efficiency factor  $Q_a(\lambda)$  for the two illustrative stations; **b**, particulate package effect  $Q_a^*(\lambda)$  for the two illustrative stations; **c**, linear relationships between package effect  $Q_a^*$  and effective radius  $r_{\text{eff}}$  at 442 nm (squares), 622 nm (circles) and 674 nm (filled triangles).

variability at all three wavelengths in  $Q_a^*$  can be explained by particle size, although it should be appreciated that the PSD spectra are used in the derivation of both  $r_{\text{eff}}$  and  $Q_a^*$  and as such they are not strictly independent. As expected,  $Q_a^*$  (442) showed the lowest correlation with  $r_{\text{eff}}$ , as the absorption of cellular material was largest in this region relative to the other two wavelengths.

The  $\bar{Q}_{b_b}$  spectra in Fig. 7a display the effects of anomalous diffraction, particularly noticeable at the offshore stations, where the range in  $\kappa(\lambda)$  values is more than twice as broad as inshore. This results in the more pronounced spectral features evident in the  $\bar{Q}_{b_b}$  spectra for the offshore station: the depressions in the  $\bar{Q}_{b_b}$  spectra are associated with peaks in the  $\kappa(\lambda)$  spectra

Table 3. Optical efficiency factors, package effect, absorption and backscattering characteristics for all samples. The shaded box indicates offshore stations.

Station / depth	Absorption efficiency factor $Q_a(674)$	Backscattering efficiency factor $Q_{bs}(550)$	Package effect factor $Q_a^*(674)$	Particulate absorption		Phytoplankton absorption		Chl-specific phytoplankton absorption $a_p^*(674)$	Particulate backscattering $b_b(550)$
				$a_p(622)$	$a_p(674)$	$a_p(622)$	$a_p(674)$		
b0202/0 m	0.09	$4.35 \times 10^{-4}$	0.97	0.044	0.118	0.044	0.118	0.037	$5.79 \times 10^{-4}$
b0202/17 m	0.08	$2.69 \times 10^{-4}$	0.95	0.046	0.113	0.040	0.107	0.037	$3.30 \times 10^{-4}$
b0202/30 m	0.05	$2.46 \times 10^{-4}$	0.97	0.035	0.084	0.034	0.082	0.038	$3.18 \times 10^{-4}$
b0202/40 m	0.17	$8.34 \times 10^{-4}$	0.90	0.008	0.010	0.008	0.010	0.053	$5.02 \times 10^{-5}$
b0302/0 m	0.21	$4.39 \times 10^{-4}$	0.92	0.051	0.131	0.051	0.131	0.034	$2.72 \times 10^{-4}$
b0302/10 m	0.12	$2.76 \times 10^{-4}$	0.93	0.046	0.120	0.043	0.116	0.032	$2.23 \times 10^{-4}$
b0302/20 m	0.23	$3.88 \times 10^{-4}$	0.86	0.021	0.051	0.021	0.050	0.050	$7.59 \times 10^{-5}$
b0302/25 m	0.25	$4.44 \times 10^{-4}$	0.85	0.020	0.046	0.019	0.045	0.041	$7.20 \times 10^{-5}$
b0401/0 m	0.26	$4.50 \times 10^{-4}$	0.82	0.092	0.220	0.092	0.220	0.015	$3.79 \times 10^{-4}$
b0402/0 m	0.14	$9.46 \times 10^{-4}$	0.92	0.061	0.161	0.061	0.161	0.025	$1.06 \times 10^{-3}$
b0402/8 m	0.16	$1.19 \times 10^{-3}$	0.90	0.067	0.168	0.062	0.163	0.026	$1.03 \times 10^{-3}$
b0402/16 m	0.09	$1.28 \times 10^{-4}$	0.95	0.032	0.078	0.029	0.076	0.024	$8.91 \times 10^{-5}$
b0402/20 m	0.09	$1.35 \times 10^{-4}$	0.95	0.025	0.054	0.020	0.051	0.028	$7.02 \times 10^{-5}$
b0502/0 m	0.13	$2.09 \times 10^{-3}$	0.93	0.011	0.024	0.011	0.024	0.037	$3.75 \times 10^{-4}$
b0502/13 m	0.16	$1.98 \times 10^{-3}$	0.91	0.010	0.030	0.008	0.029	0.050	$3.18 \times 10^{-4}$
b0502/28 m	0.14	$1.65 \times 10^{-3}$	0.92	0.009	0.028	0.008	0.027	0.046	$3.20 \times 10^{-4}$
b0503/0 m	0.22	$3.94 \times 10^{-4}$	0.91	0.012	0.032	0.012	0.032	0.049	$5.61 \times 10^{-5}$
b0503/13 m	0.10	$2.24 \times 10^{-4}$	0.94	0.011	0.029	0.009	0.029	0.049	$5.65 \times 10^{-5}$
b0503/28 m	0.09	$2.00 \times 10^{-4}$	0.95	0.011	0.027	0.011	0.027	0.045	$4.99 \times 10^{-5}$
b0601/0 m	0.24	$1.02 \times 10^{-3}$	0.82	0.010	0.028	0.010	0.028	0.044	$1.17 \times 10^{-4}$
b0701/0 m	0.07	$4.95 \times 10^{-4}$	0.98	0.009	0.021	0.009	0.021	0.035	$1.50 \times 10^{-4}$
b0801/0 m	0.39	$1.22 \times 10^{-4}$	0.70	0.053	0.122	0.053	0.122	0.021	$3.85 \times 10^{-5}$
b0802/0 m	0.38	$1.56 \times 10^{-4}$	0.79	0.052	0.128	0.052	0.128	0.024	$5.31 \times 10^{-5}$
Minimum	0.05	$1.22 \times 10^{-4}$	0.70	0.008	0.010	0.008	0.010	0.015	$3.85 \times 10^{-5}$
Maximum	0.39	$2.09 \times 10^{-3}$	0.98	0.092	0.220	0.092	0.220	0.053	$1.06 \times 10^{-3}$
Mean (s.d.) inshore	0.18 (0.10)	$4.69 \times 10^4 (3.33 \times 10^4)$	0.89 (0.08)	0.040 (0.023)	0.097 (0.058)	0.038 (0.023)	0.097 (0.058)	0.033 (0.010)	$2.88 \times 10^4 (3.20 \times 10^4)$
Mean (s.d.) offshore	0.14 (0.05)	$1.09 \times 10^3 (9.07 \times 10^4)$	0.92 (0.02)	0.011 (0.001)	0.028 (0.003)	0.028 (0.003)	0.010 (0.002)	0.046 (0.005)	$1.96 \times 10^4 (1.57 \times 10^4)$

(Fig. 5b). The influence of higher  $n(\lambda)$  values in the enhanced magnitude of backscatter<sup>9</sup> can also be seen. The surface inshore samples displayed backscattering efficiencies ( $1+\epsilon = 1.043, 1.045$ ) almost an order of magnitude higher than the deeper inshore samples ( $1+\epsilon = 1.023, 1.024$ ). Figure 7b shows the relationship between  $\bar{Q}_{b_b}$  and the real part of the refractive index, given by the central value  $1+\epsilon$ , for the three wavelengths previously used. Only the 17 samples that produced model convergences were used in these regressions. The real part of the refractive index exerts a strong influence upon scattering<sup>9</sup> (it could be argued that it is causal), thus it is not surprising that strong correlations between  $1+\epsilon$  and  $\bar{Q}_{b_b}$  were observed for all three wavelengths. However, backscattering is also influenced by particle size and  $\kappa(\lambda)$ , so to be able to explain 90–96% of backscattering variability through one refractive index parameter is perhaps unexpected. The influence of higher  $\kappa$  values at 442 nm can be invoked to explain the lower correlation between  $1+\epsilon$  and  $\bar{Q}_{b_b}$  observed at these wavelengths. Figure 7c shows similar relationships, this time using the ratio of  $\bar{Q}_{b_b}/\bar{Q}_a$  for the three wavelengths. The introduction of absorption effects produces a lower correlation between  $1+\epsilon$  and  $\bar{Q}_{b_b}/\bar{Q}_a$  relative to  $1+\epsilon$  and  $\bar{Q}_{b_b}$ , but it is still highly significant ( $r^2 = 0.82-0.90, n = 17, P < 0.0005$ ). It can be seen that the highest correlation was produced at 622 nm: this is consistent with lower absorption in this region of the spectrum.

Absorption and backscattering coefficients

The potential application of the good correlation between  $1+\epsilon$  and  $\bar{Q}_{b_b}/\bar{Q}_a$  lies in the relationship, derived from Equation (3):

$$\frac{\bar{Q}_{b_b}}{\bar{Q}_a} = \frac{b_b}{a} \tag{9}$$

Equation (9) has two characteristics that are useful. First, it allows an analysis of the bulk optical coefficients with respect to the optical efficiency factors. Given the relationship established in Fig. 7c, this means that there is potential to derive the real part of the refractive index from a ratio of  $b_b/a$ . Second, the ratio  $b_b/a$  is a product of ocean colour reflectance models,<sup>16</sup> with the further implication that there is potential to calculate the real part of the refractive index from ocean colour measurements. The correlation between  $b_b(622)$  and  $1+\epsilon$ , while still significant, is low ( $r^2 = 0.57, n = 17,$

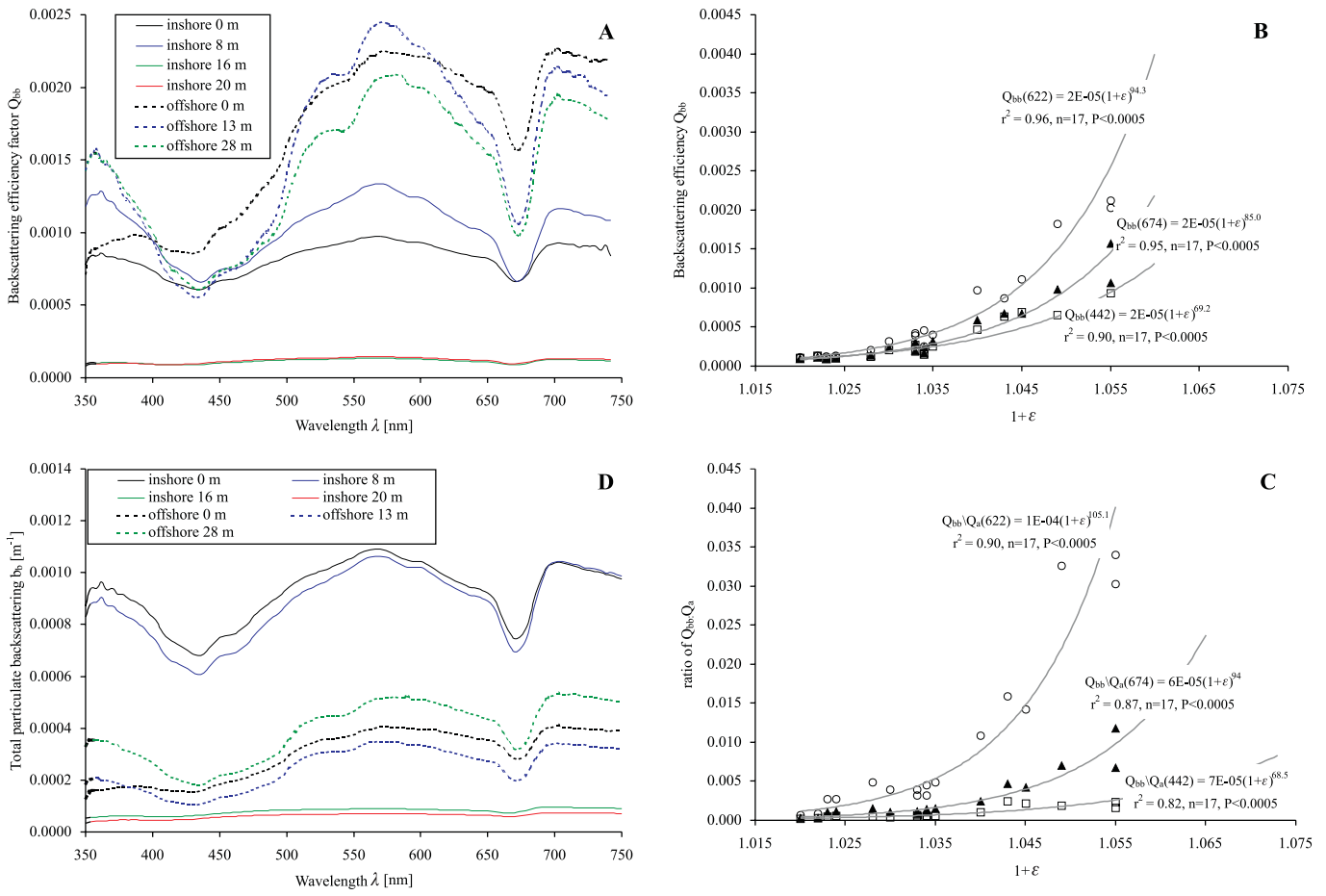


**Fig. 7.** Backscattering characteristics and influences: **a**, mean particulate backscattering efficiency factors  $\bar{Q}_{bb}(\lambda)$  for the two illustrative stations; **b**, power law relationships between  $\bar{Q}_{bb}(\lambda)$  and the central value of the real part of the refractive index  $1+\varepsilon$  at 442 nm (squares), 622 nm (circles) and 674 nm (filled triangles); **c**, power law relationships between the ratio  $\bar{Q}_{bb}/\bar{Q}_a$  and the central value of the real part of the refractive index  $1+\varepsilon$  at 442 nm (squares), 622 nm (circles) and 674 nm (filled triangles); and **d**, total particulate backscattering coefficients  $b_b(\lambda)$  for the two illustrative stations.

$P < 0.01$ ), owing to the added influence of the particle size distribution on  $b_b$ . As expected from Equation (9), the correlation between  $b_b/a$  and  $1+\varepsilon$  is equivalent to that between  $\bar{Q}_{bb}/\bar{Q}_a$  and  $1+\varepsilon$  ( $r^2 = 0.82$  to  $0.90$ ,  $n = 17$ ,  $P < 0.0005$ ). Tabulated values of particulate absorption and backscattering for all samples are given in Table 3.

Particulate backscattering spectra are displayed in Fig. 7d, with epitomized values in Table 3. The combined effects of the optical efficiency factor  $\bar{Q}_{bb}$  (Fig. 6d), and the particle size distribution (Fig. 4) are evident when comparing the surface inshore, deep inshore and all offshore samples. Despite the lower  $\bar{Q}_{bb}$  values of surface inshore samples in comparison to offshore, the greater number of particles (chl *a* values are an order of magnitude higher) resulted in  $b_b$  values approximately twice as high. However, the deeper inshore stations, despite having chl *a* values three to six times higher than offshore, display  $b_b$  spectra lower in magnitude; this results from the much higher offshore  $\bar{Q}_{bb}$  values. The correlation between  $b_b$  and the real part of the refractive index has already been shown to be low, and given the added influence of the PSD upon  $b_b$ , it appears that the backscattering efficiency factor  $\bar{Q}_{bb}$  offers a simpler means of analysing the effects of refractive index on backscattering processes.

The relationship between chl *a* and phytoplankton absorption is typically used in bio-optical algorithms to link algal optics to gross pigment biomass.<sup>33</sup> Figure 8a shows a power law-based correlation<sup>34</sup> between particulate absorption at 622 nm and at 674 nm, and chl *a* concentration. Stuart *et al.*<sup>35</sup> argued that 622 nm

is an optimal wavelength for the determination of chl *a* from absorption, as package effects are lowest in this part of the spectrum. The 674-nm wavelength was used because chl *a* is the only pigment that absorbs in this spectral region.<sup>30</sup> Absorption at both wavelengths was highly correlated with chl *a* (Fig. 8a) and it appeared that there was little to choose between the two wavelengths statistically.

Interestingly, if detritally corrected phytoplankton absorption is used instead of particulate absorption to establish these relationships, the correlation is not improved. This indicates the advantage of using higher wavelength absorption values for chl *a* determination, where detrital absorption is minimal.<sup>18</sup> However, although the MERIS sensor does have an anticipated band at 620 nm, neither the SeaWiFS (Sea viewing Wide Field of view Sensor) nor MODIS (MODerate resolution Imaging Spectrometer) sensors have such a band.<sup>32</sup>

Absorption spectra of chlorophyll *a*-specific phytoplankton  $a^*_\phi(\lambda)$  for the sample stations are displayed in Fig. 8b, with values for all samples given in Table 3. Phytoplankton (as opposed to particulate) absorption has been corrected for detrital absorption,<sup>18</sup> which constitutes 5–40% of total absorption at 442 nm, 0–19% of total absorption at 622 nm, and 0–6% of total absorption at 674 nm. Again there is a difference in structure between offshore and inshore algal communities (Fig. 8b), with offshore samples displaying  $a^*_\phi(\lambda)$  values  $\sim 2$ –3 times higher than inshore. This is the case if all samples are considered, and in addition indicates that inshore sites displayed greater variability in  $a^*_\phi(\lambda)$

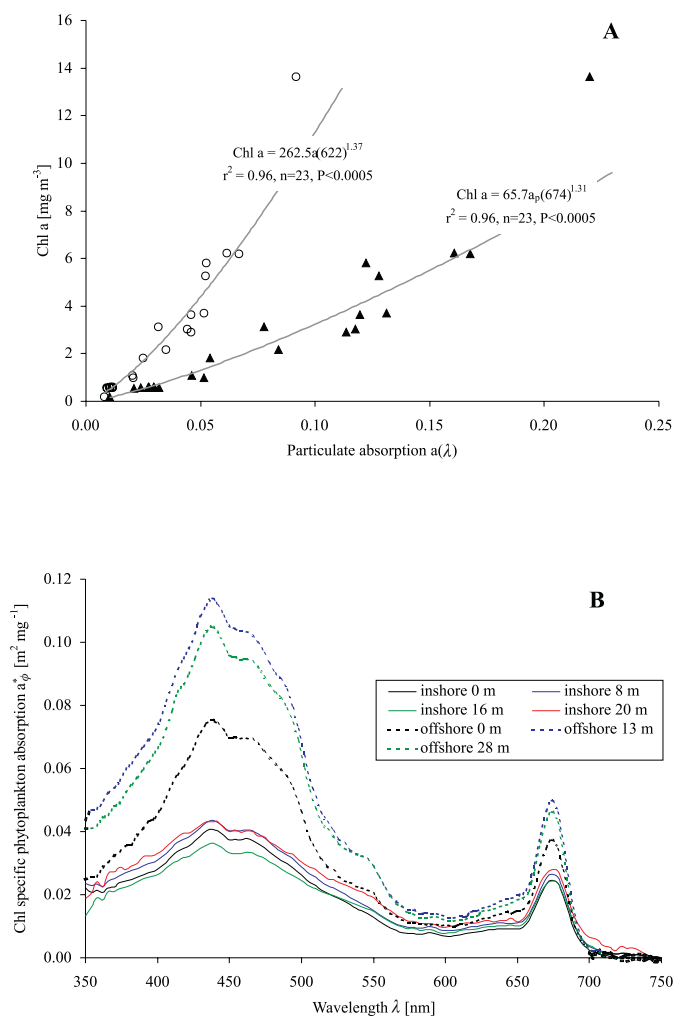


**Fig. 8.** Particulate absorption and chlorophyll a concentrations: **a**, power law relationships between particulate absorption  $a_p(\lambda)$  and chlorophyll a concentrations at 622 nm (circles) and 674 nm (filled triangles), for all samples; **b**, chlorophyll a-specific phytoplankton absorption  $a^*_\phi(\lambda)$  for the two illustrative stations. These spectra have been corrected for detrital absorption.

(Table 3). The decrease in  $a^*_\phi(\lambda)$  values as trophic state changes from offshore waters to inshore coastal waters has been demonstrated elsewhere.<sup>34</sup> As discussed previously, the probable effects of phycoerythrin absorption can be seen at ~550 nm in the offshore samples. The magnitude of  $a^*_\phi(674)$  allows some analysis of the methods used to determine absorption,<sup>34</sup> as a theoretical maximum for this value can be determined. Johnsen *et al.*<sup>36</sup> measured a maximal value of  $a^*_\phi(675) = 0.027$  for unpacked, intact chl a containing chromoproteins; this value can be considered to represent a theoretical maximum for  $a^*_\phi(674)$  with no package effect, in a spectral region where there is minimal absorption from other pigments.<sup>36</sup> The range of  $a^*_\phi(674)$  values in this data set (0.015–0.053 m<sup>2</sup> mg<sup>-1</sup>, mean = 0.036 m<sup>2</sup> mg<sup>-1</sup>, s.d. = 0.011) indicate that many  $a^*_\phi(674)$  values reported here surpass this theoretical maximum (17 of the 23 samples). The effects of chlorophyll b at this wavelength is small<sup>30</sup> and there is little evidence of significant phaeopigment absorption in any of the samples (R.G. Barlow, unpubl. obs.). The high  $a^*_\phi(674)$  values seen here are thus indicative of some methodological uncertainties: previous publications also displayed such a phenomenon, which is ascribed to uncertainties in the pathlength amplification factor.<sup>34</sup>

**Conclusions**

This study demonstrated that variability in algal community structure can be detected by means of various optical properties. These range from the causal mechanisms of particle optics such as refractive index and particle size, through mean optical efficiency factors, to the bulk absorption and backscattering coefficients. The ability to examine all aspects of the optical properties of algal assemblages allows an appreciation of cause, effect and the potential utility of algal optical signals in the interpretation of ocean colour data.

The inverse anomalous diffraction model described here has the ability, under certain conditions, to determine spectral values of both the real and imaginary part of the algal refractive index from contributions of measured particulate absorption and particle size distributions. These conditions appear to be primarily controlled by the particle size distribution as described by the effective radius  $r_{eff}$  and effective variance  $v_{eff}$ . The model operates most effectively if the particle population is not widely dispersed ( $v_{eff}$  is relatively low at <2.3) and is more likely to produce unequivocal returns if the mean particle size is relatively small ( $r_{eff} < 5 \mu\text{m}$ ). These findings are consistent with previous studies.<sup>7,8</sup> The utility of the KK relations in quantifying the relationship between the real and imaginary parts of the refractive index was also demonstrated: the essentially simple and fast computation of these relations has potential application in the inverse iterative determination of algal bulk optical coefficients.

The value of the real part of the refractive index was demonstrated as a descriptor of algal community structure. The application in this study is restricted to distinguishing coastal diatom-dominated communities from oligotrophic pyrmnesiophyte and chlorophyte-dominated assemblages. The real part of the refractive index  $1 + \epsilon$  and the backscattering efficiency factor  $\bar{Q}_{b_b}$  are shown to be highly correlated using a power law function. Such a relationship allows prediction of  $1 + \epsilon$  from a ratio of the optical efficiency factors  $\bar{Q}_{b_b} / \bar{Q}_{a'}$ , and thus from the equivalent ratio of  $b_b/a$ . This has potential application in inverse reflectance models,<sup>33,16</sup> and offers the possibility of distinguishing algal communities, based on refractive index, from ocean colour data.

The numerical expression derived here for the  $(1 + \epsilon):b_b/a$  relationship is only of relevance to the small data set analysed in this study. A robust relationship is also observed between gross biomass as given by chl a concentrations, and particulate absorption at 622 nm.<sup>35</sup> Such a relationship offers application with the MERIS sensor as the link between algal optics derived from inverse reflectance models and chl a concentrations.

The assistance of August Miller with the Mie modelling, and funding by Marine and Coastal Management, the National Research Foundation and BENEFIT are gratefully acknowledged.

Received 20 July 2000. Accepted 14 June 2001.

- Morel A. (1980). In-water and remote measurements of ocean color. *Boundary-Layer Meteorol.* **18**, 177–202.
- Priesendorfer R.W. (1961). Application of radiative transfer theory to light measurements in the sea. *Int. Geophys. Deod. Monogr.* **10**, 11–29.
- Yentsch C.S. (1962). Measurement of visible light absorption by particulate matter in the ocean. *Limnol. Oceanogr.* **7**, 207–217.
- Mitchell B.G. (1990). Algorithms for determining the absorption coefficient of aquatic particulates using the quantitative filter technique (QFT). In *SPIE Proceedings Vol. 1302, Ocean Optics X*, ed. R.W.Spinrad, pp. 137–148. Society for Photo-Optical Instrumentation Engineers, Bellingham, Washington.
- Ahn Y-H, Bricaud A. and Morel A. (1992). Light backscattering efficiency and related properties of some phytoplankters. *Deep-Sea Res.* **39A**, 1835–1855.
- Van de Hulst H.C. (1957). *Light Scattering by Small Particles*. Wiley, New York.
- Bricaud A. and Morel A. (1986). Light attenuation and scattering by phytoplanktonic cells: a theoretical modeling. *Appl. Opt.* **25**, 571–580.

8. Stramski D., Morel A. and Bricaud A. (1988). Modelling the light attenuation and scattering by spherical phytoplankton cells: a retrieval of the bulk refractive index. *Appl. Opt.* **27**, 2954–3956.
9. Morel A. and Bricaud A. (1986). Inherent properties of algal cells including picoplankton: theoretical and experimental results. *Can. Bull. Fish. Aquat. Sci.* **214**, 521–559.
10. Stramski D. and Kiefer D.A. (1991). Light scattering by micro-organisms in the open ocean. *Prog. Oceanogr.* **28**, 343–383.
11. Aas E. (1996). Refractive index of phytoplankton derived from its metabolite composition. *J. Plank. Res.* **18**, 2223–2249.
12. Stramski D. (1999). Refractive index of planktonic cells as a measure of cellular carbon and chlorophyll *a* content. *Deep-Sea Res.* **46**, 335–351.
13. Quinby-Hunt M.S., Hunt A.J., Lofftus K. and Shapiro D. (1989). Polarized-light scattering studies of marine *Chlorella*. *Limnol. Oceanogr.* **34**, 1587–1600.
14. Volten H., de Haan J.E., Hovenier J.W., Schreurs R., Vassen W., Dekker A.G., Hoogenboom H.J., Charlton F. and Wouts R. (1998). Laboratory measurements of angular distributions of light scattered by phytoplankton and silt. *Limnol. Oceanogr.* **43**, 1180–1197.
15. Carder K.L., Chen E.R., Lee Z.P., Hawes S. and Kamykowski D. (1999). Semi-analytic MODIS algorithms for chlorophyll *a* and absorption with bio-optical domains based on nitrate-depletion temperatures. *J. Geophys. Res.* **104**, 5403–5421.
16. Roesler C.S. and Perry M.J. (1995). *In situ* phytoplankton absorption, fluorescence emission, and particulate backscattering spectra determined from reflectance. *J. Geophys. Res.* **C100**, 13 279–13 294.
17. Roesler C.S. (1998). Theoretical and experimental approaches to improve the accuracy of particulate absorption coefficients derived from the quantitative filter technique. *Limnol. Oceanogr.* **43**, 1649–1660.
18. Kishino M., Takahashi M., Okami N. and Ichimura S. (1985). Estimation of the spectral absorption coefficients of phytoplankton in the sea. *Bull. Mar. Sci.* **37**, 634–642.
19. Bader H. (1970). The hyperbolic distribution of particle sizes. *J. Geophys. Res.* **75**, 2822.
20. Jonasz M. and Fournier G. (1996). Approximation of the size distribution of marine particles by a sum of log-normal functions. *Limnol. Oceanogr.* **41**, 744–754.
21. Hansen J.E. and Travis L.D. (1974). Light scattering in planetary atmospheres. *Space. Sci. Rev.* **16**, 527–610.
22. Mishchenko M.I., Travis L.D., Kahn R.A. and West R.A. (1997). Modeling phase functions for dustlike tropospheric aerosols using a shape mixture of randomly oriented polydisperse spheroids. *J. Geophys. Res.* **102**, 16 831–16 847.
23. Barlow R.G., Aiken J., Sessions H.E., Lavender S. and Mantel J. (2001). Phytoplankton pigment, absorption and ocean colour characteristics in the southern Benguela ecosystem. *S. Afr. J. Sci.* **97**, 230–238.
24. Bohren C.F. and Huffman D.R. (1983). *Absorption and Scattering of Light by Small Particles*. Wiley, New York.
25. Bricaud A., Bedhomme A.L. and Morel A. (1988). Optical properties of diverse phytoplanktonic species: experimental results and theoretical interpretation. *J. Plank. Res.* **10**, 851–873.
26. Mobley, C.D. (1994). *Light and Water: Radiative Transfer in Natural Waters*. Academic Press, San Diego.
27. Wiscombe W. (1996). Mie Scattering Calculations — Advances in technique and fast, vector-speed computer codes. *NCAR Tech Note TN-140+STR*, revised edn. National Center for Atmospheric Research, Boulder, Colorado.
28. Morel A. and Bricaud A. (1981). Theoretical results concerning light absorption in a discrete medium, and application to specific absorption of phytoplankton. *Deep-Sea Res.* **28**, 1375–1393.
29. McCave I.N. (1983). Particulate size spectra, behavior, and origin of nepheloid layers over the Nova Scotian continental rise. *J. Geophys. Res.* **C88**, 7647–7666.
30. Jeffrey S.W., Mantoura R.F.C. and Wright S.W. (1997). *Phytoplankton Pigments in Oceanography: Guidelines to Modern Methods*. Monographs on Oceanographic Methodology **10**, UNESCO, Paris.
31. Kirk J.T.O. (1975). A theoretical analysis of the contribution of algal cells to the attenuation of light within natural waters. II. Spherical cells. *New. Phytol.* **75**, 21–36.
32. IOCCG. (1998). *Minimum Requirements for an Operational Ocean-colour Sensor for the Open Ocean*. Reports of the International Ocean Colour Co-ordinating Group, Dartmouth, Canada.
33. Garver S.A. and Siegel D.A. (1997). Inherent optical property inversion of ocean color spectra and its biogeochemical interpretation. 1: Time series from the Sargasso Sea. *J. geophys. Res.* **102**, 18 607–18 625.
34. Bricaud A., Babin M., Morel A. and Claustre H. (1995). Variability in the chlorophyll-specific absorption coefficients of natural phytoplankton: analysis and parameterization. *J. geophys. Res.* **100**, 13 321–13 332.
35. Stuart V., Sathyendranath S., Platt T., Maass H. and Irwin B.D. (1998). Pigment and species composition of natural phytoplankton populations: effect on the absorption spectra. *J. Plankt. Res.* **20**, 187–217.
36. Johnsen G., Nelson N.B., Jovine R.V.M. and Prezelin B.B. (1994). Chromo-protein- and pigment-dependent modelling of spectral light absorption in two dinoflagellates, *Prorocentrum minimum* and *Heterocapsa pygmaea*. *Mar. Ecol. Prog. Ser.* **114**, 245–258.
37. Hocutt C.H. and Verheye H.M. (2001). BENEFIT marine science in the Benguela Current during 1999: Introduction. *S. Afr. J. Sci.* **97**, 195–198.

## Wits rock art archive to go online

Benjamin Smith\*

DURING THE LAST 21 YEARS, THE ROCK ART RESEARCH INSTITUTE (RARI) at the University of the Witwatersrand built up one of the largest rock art archives in the world. Thanks to a generous donation from the Ringing Rocks Foundation in New York, these archives are now being digitized and, once the process is complete, the collections will be placed online.

Digitization is expected to take three years and will create three new jobs. More than 2000 large paper copies and drafting film tracings/redrawings will be scanned in plastic carrier using a large-format Contex<sup>®</sup> scanner, 50 inches (127 cm) in width. This scanner is able to take even the largest RARI paper records such as Harald Pager's Ndedema copies. The images will be scanned at actual size and to a resolution of 800 dots per inch. More than 150 000 photographs, slides (of all formats), bromides and historic documents will be scanned on a Scitex<sup>®</sup> flatbed scanner capable of 14 000 dpi. A maximum of 250 megabytes will be allocated for each piece. For a 35-mm slide this means in practice that scanning will be at approximately 200 dpi at A0 size. Full-resolution scans of all images will then be burnt to DVD and stored in a dedicated archive according to international standards.

Thumbnails and A4 images of each piece in the collections will be placed onto banks of hard-drives and placed online.

A database software package called Index+<sup>®</sup> will be used to store and access the digital archive. This software package has sophisticated search facilities and is designed to be viewed on standard web browsers. Remote users will thus be able search the collections from their offices and homes using Microsoft Explorer<sup>®</sup> and Netscape<sup>®</sup> browsers.

RARI supports the South African Archaeological Association's code of conduct on the publication of site location details and will therefore place access restrictions upon sensitive parts of the database.

The institute is willing to consider requests from other institutions within southern Africa that would like to use its facilities to digitise their rock art recordings and archival collections. Preference will be given based on the urgency of the need for digitization.



Getting the picture: soon these images will be accessible by your personal computer, thanks to a generous donation from an American foundation.

\*Rock Art Research Institute, University of the Witwatersrand, Private Bag 3, WITS, 2050 South Africa. E-mail: 107bws@cosmos.wits.ac.za